

See discussions, stats, and author profiles for this publication at: <https://www.researchgate.net/publication/262230184>

Super-Stable, Highly Monodisperse Plasmonic Faradaurate-500 Nanocrystals with 500 Gold Atoms: Au ~500 (SR) ~120

ARTICLE in JOURNAL OF THE AMERICAN CHEMICAL SOCIETY · MAY 2014

Impact Factor: 12.11 · DOI: 10.1021/ja502327a · Source: PubMed

CITATIONS

16

READS

74

6 AUTHORS, INCLUDING:



Xiaobing Zuo

Argonne National Laboratory

96 PUBLICATIONS 2,070 CITATIONS

[SEE PROFILE](#)



J. Ilavsky

Argonne National Laboratory

222 PUBLICATIONS 3,164 CITATIONS

[SEE PROFILE](#)



Karena W Chapman

Argonne National Laboratory

163 PUBLICATIONS 3,505 CITATIONS

[SEE PROFILE](#)



Amala Dass

University of Mississippi

108 PUBLICATIONS 3,277 CITATIONS

[SEE PROFILE](#)

Super-Stable, Highly Monodisperse Plasmonic Faradaurate-500 Nanocrystals with 500 Gold Atoms: $\text{Au}_{\sim 500}(\text{SR})_{\sim 120}$

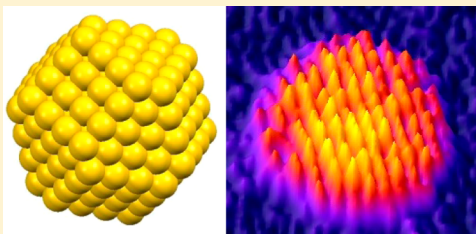
Chanaka Kumara,[†] Xiaobing Zuo,[‡] Jan Ilavsky,[‡] Karena W. Chapman,[‡] David A. Cullen,[§] and Amala Dass*,[†]

[†]Department of Chemistry and Biochemistry, University of Mississippi, Oxford, Mississippi 38677, United States

[‡]X-ray Science Division, Advanced Photon Source, Argonne National Laboratory, Argonne, Illinois 60439, United States

[§]Materials Science and Technology Division, Oak Ridge National Laboratory, Oak Ridge, Tennessee 37831, United States

ABSTRACT: Determining the composition of plasmonic nanoparticles is challenging due to a lack of tools to accurately quantify the number of atoms within the particle. Mass spectrometry plays a significant role in determining the nanoparticle composition at the atomic level. Significant progress has been made in understanding ultrasmall gold nanoparticles such as $\text{Au}_{25}(\text{SR})_{18}$ and $\text{Au}_{38}(\text{SR})_{24}$, which have Au core diameters of 0.97 and 1.3 nm, respectively. However, progress in 2–5 nm-diameter small plasmonic nanoparticles is currently impeded, partially because of the challenges in synthesizing monodisperse nanoparticles. Here, we report a plasmonic nanocrystal that is highly monodisperse, with unprecedentedly small size variability. The composition of the superstable plasmonic nanocrystals at 115 kDa was determined as $\text{Au}_{500 \pm 10}(\text{SR})_{120 \pm 3}$. The $\text{Au}_{\sim 500}$ system, named Faradaurate-500, is the largest system to be characterized using high resolution electrospray (ESI) mass spectrometry. Atomic pair distribution function (PDF) data indicate that the local atomic structure is consistent with a face-centered cubic (fcc) or Marks decahedral arrangement. High resolution scanning transmission electron microscopy (STEM) images show that the diameter is 2.4 ± 0.1 nm. The size and the shape of the molecular envelope measured by small-angle X-ray scattering (SAXS) confirms the STEM and PDF analysis.



$\text{Au}_{500 \pm 10}(\text{SR})_{120 \pm 3}$
115 kDa, 2.4 nm

INTRODUCTION

Surface plasmon resonance (SPR) is the light-induced collective oscillation of conduction electrons, with applications in photochemistry,¹ solar cells,^{2–5} and biomedical areas including cancer cell detection, drug delivery, and chemical sensing.⁶ Gold shows SPR in nanoparticles as small as 2 nm diameter, at wavelengths of 500–550 nm, which red shifts with increasing nanoparticle size and aspect ratio. Nanoscale gold particles can be synthesized with different sizes⁷ (up to 100 nm) and a rich variety of shapes^{8,9} (e.g., prism, cubic, hexagonal, hollow), all of which can be used to tune the SPR.

Characterization of citrate-protected colloidal gold nanoparticles (<5 nm), where molecule-to-plasmonic transitions occur, is limited by sample polydispersity and instability, with particle aggregation often observed on short time scales. Ultrastable gold nanoparticles have previously been prepared by protecting the nanoparticle core with thiolates using the Brust–Schrifflin method.¹⁰ The dispersity of the Brust–Schrifflin product can be enhanced by a thermochemical treatment.¹¹ This produces atomically monodisperse Au-SR molecules (SR = thiolate), like $\text{Au}_{25}(\text{SR})_{18}$, $\text{Au}_{38}(\text{SR})_{24}$, and $\text{Au}_{144}(\text{SR})_{60}$, which are stable in air, at high temperature (~ 80 °C), and under humid conditions. Concurrently, advances in instrumental methods have developed mass spectrometry (MS) as a valuable tool to identify nanoparticles via compositional analysis.¹² This is because transmission electron microscopy

(TEM) characterization remains a challenge at smaller nanoparticle sizes (<3 nm diameter) due to rapid electron beam-induced damage, though limited success is achievable. Specifically, progress in electrospray ionization (ESI) mass spectrometry with multiply charged molecular ions and matrix-assisted laser desorption ionization mass spectrometry (MALDI-MS) with DCTB matrix¹³ enabled the compositional assignment of these ultrasmall nanoparticles.^{14,15} This has enabled successful identification of various gold,¹⁶ silver,¹⁷ and alloy^{18,19} nanomolecules using mass spectrometry. However, evaluating the composition of larger plasmonic nanoparticles (>2 nm diameter, >300– atoms) is still impeded by limitations in ionization and detection of molecular ions.

For ultrasmall thiol-protected gold nanoparticles, which can be isolated as single crystals, fundamental understanding has been facilitated by structural analysis using X-ray crystallography. For such ultrasmall systems, the small particle size and particle uniformity are critical to isolating single crystals. Thiol-protected nanoparticles as large as $\text{Au}_{102}(\text{S}-\text{Ph}-\text{COOH})_{44}$ have been crystallographically characterized,²⁰ with several other Au nanoparticle crystal structures containing less than 102 gold atoms also being reported.^{21–23} However, atomic structural analysis of plasmonic nanoparticles remains challenging, with

Received: March 6, 2014

Published: May 9, 2014

the larger particle size and increased polydispersity often preventing crystallization. In such cases, atomic pair distribution function (PDF) analysis of high energy synchrotron-based X-ray total scattering data can provide atomic-scale structural information, with crystallographic resolution independent of the sample crystallinity.

Here we report the preparation of highly monodisperse plasmonic nanoparticles containing ~ 500 ($\pm 2\%$) Au atoms. We name the $\text{Au}_{500 \pm 10} \text{SR}_{120 \pm 3}$ system “Faradaurate-500”, in honor of Michael Faraday.²⁴ Compared to similarly sized colloidal plasmonic nanoparticles, where the term “monodisperse” is generally applied to a system with ca. 10% standard deviation, the ± 10 Au atom variability reported here is unmatched for systems of this size. We report the MALDI and ESI mass spectrometry at unprecedented high mass for nanoparticle characterization at 115 and 38 kDa, respectively. Furthermore, we employed synchrotron X-ray and high resolution electron microscopy to study the atomic structure. In a preliminary report on the 76.3 kDa Faradaurate nanomolecules, we mentioned that other stable sizes exists at 114 and 207 kDa.²⁴ Here we present a detailed study on local structure, size, and size uniformity and report its composition as $\text{Au}_{500 \pm 10} \text{SR}_{120 \pm 3}$. High-energy X-ray scattering-based atomic PDF analysis shows that the atoms are in a cubic close packing (fcc) or Marks decahedron arrangement. The extent of features in the PDF, to 24 Å, suggests a 2.4 nm diameter nanoparticle. Aberration-corrected high-angle annular dark-field scanning transmission electron microscopy (HAADF-STEM) images of the particles show the size, shape, and core morphology of thiol protected plasmonic gold nanoparticles with atomic resolution. Low-magnification STEM images presenting an ensemble of particles show a uniform size distribution in the 2.4 ± 0.1 nm range, and self-assembled regions visually indicating size uniformity. Furthermore, small-angle X-ray scattering data yield a diameter of 2.6 ± 0.2 nm. SAXS data also shows an oscillatory behavior indicating high monodispersity. Structural information in PDF analysis allowed us to obtain a model for the Au core. Calculated PDFs of a Au_{405} truncated-octahedral core and a Au_{389} Marks decahedron provide good matches with the experimental data. A variety of complementary characterization techniques yield information about composition, size, size distribution, and atomic structure. The $\text{Au}_{500 \pm 10} \text{SR}_{120 \pm 3}$ nanoparticles have a core diameter of 2.4 nm, with the ± 10 atoms polydispersity corresponding to <0.1 nm variability in diameter. Not only can such highly monodisperse plasmonic nanocrystals facilitate the fundamental understanding of evolution of atomic and electronic structure with size, but these also have diverse potential applications.

EXPERIMENTAL SECTION

Synthesis. Synthesis involves three steps. First, a crude product containing polydisperse Au clusters was prepared in a modification of a reported process.²⁴ Second, thermochemical treatment of the crude product with excess thiol was applied to eliminate metastable clusters. Finally, solvent fractionation was used to isolate pure monodisperse nanomolecules.

Aqueous solution (30 mL) containing HAuCl_4 (0.1772 g/0.45 mmol) was mixed with toluene solution (30 mL) of tetraoctylammonium bromide, TOABr (0.55 mmol). After stirring for 30 min, the organic phase was separated, and phenylethanethiol (0.0622 mL/0.225 mmol) was added and further stirred for 30 min at room temperature (gold to thiol molar ratio was set to 1:0.5). This solution was cooled in an ice bath for 30 min. An aqueous solution of NaBH_4 (10 mmol, 20 mL) cooled to 0 °C, was rapidly added to the reaction mixture under

vigorous stirring. After 2 h, the organic layer was separated and evaporated to dryness. The product was washed with methanol to remove other byproducts. The residual mixture was extracted with toluene.

~ 100 mg of crude product was dissolved in 0.50 mL of toluene and subjected to thermochemical treatment with excess phenylethanethiol (0.50 mL) at 80 °C under stirring, while monitoring with MALDI-MS. After metastable clusters disappeared (~ 4 to 7 days), the product was isolated, washed with methanol several times, and extracted with toluene.

There were several types of nanomolecules in the product, 36 (major fraction), 76.3, and 115 kDa. Solvent fractionation was used to isolate the 115 kDa portion.

Mass Spectrometry. MALDI mass spectra were acquired using Bruker AutoFlex 1 and using DCTB matrix.¹³ ESI-MS was measured using Waters Synapt HDMS instrument and sample mixed with 50:50 toluene: CH_3CN or 50:50 THF: CH_3CN solvent system. $\text{Au}_{25}(\text{SCH}_2\text{CH}_2\text{Ph})_{18}$ and $\text{Au}_{144}(\text{SCH}_2\text{CH}_2\text{Ph})_{60}$ were used for calibration checks.

STEM Analysis. Specimens were prepared for STEM analysis by drop casting a suspension of particles in toluene onto lacey carbon films supported on 3 mm Cu grids. Specimens were imaged in a JEOL JEM-2200FS with a CEOS aberration corrector on the probe-forming system. Because the particles proved to be sensitive to the electron beam, images were recorded with a probe current of 13 pA and dwell time of $32 \mu\text{s}$ to limit beam dose. At higher magnification, neighboring particles were prone to rapid necking and coalescence. Thus, for particle counting analysis, areas of well-separated particles were chosen, and coalesced particles were excluded from the counting statistics. While cooling the particles in a cryogenic holder slightly improved particle stability, this was not routinely used to obtain images for particle counts.

High Energy X-ray and Pair Distribution Function (PDF) Analysis. The total scattering data suitable for PDF analysis were collected at beamline 11-ID-B at the Advanced Photon Source at Argonne National Laboratory for samples loaded in polyimide tubing of ~ 1 mm diameter. A large area detector (PerkinElmer amorphous silicon) was combined with high energy X-rays ($\lambda = 0.2128 \text{ \AA}$, $E \sim 58$ keV) to collect data to high values of momentum transfer (Q). The two-dimensional images were reduced to one-dimensional diffraction data as a function of Q within fit2d. The data were corrected for background and Compton scattering within pdfgetX2 as described previously.^{37,38} Fourier transform of the data to $Q_{\max} = 22 \text{ \AA}^{-1}$ gave the PDFs, $G(r)$. The calculated atomic PDF and PDF fitting was performed using PDFgui.³⁷

Small Angle X-ray Scattering. The SAXS data were obtained using the 12-ID-B beamline at the Advanced Photon Source at Argonne National Laboratory with an X-ray energy of 12 keV. The beamline is equipped with a Pilatus 2 M detector housed within an evacuated flight tube. This provides very low background and noise levels, and, therefore, high sensitivity of the instrument. The beam size was 0.2×0.2 mm with exposure times of 1 s. The data were corrected, background subtracted and reduced to intensity vs scattering vector (q) profiles. The data analysis was performed within the Irena SAS package.³⁹

RESULTS AND DISCUSSION

Mass Spectrometry. The composition of the Faradaurate-500 was determined using MALDI and ESI mass spectrometry. The red and blue curves in Figure 1 show the MALDI and ESI-MS spectra of the purified nanoparticles, featuring a mass at 115 kDa. MALDI shows broad peaks at 115 and 57 kDa, which are the singly and doubly charged ions of the Faradaurate-500. The breadth of these features is associated with the resolution limits of the MALDI-TOF (time-of-flight) tube at high mass range and also fragmentation/ligand loss in the laser beam. The MALDI does show the purity of isolated nanocrystals.

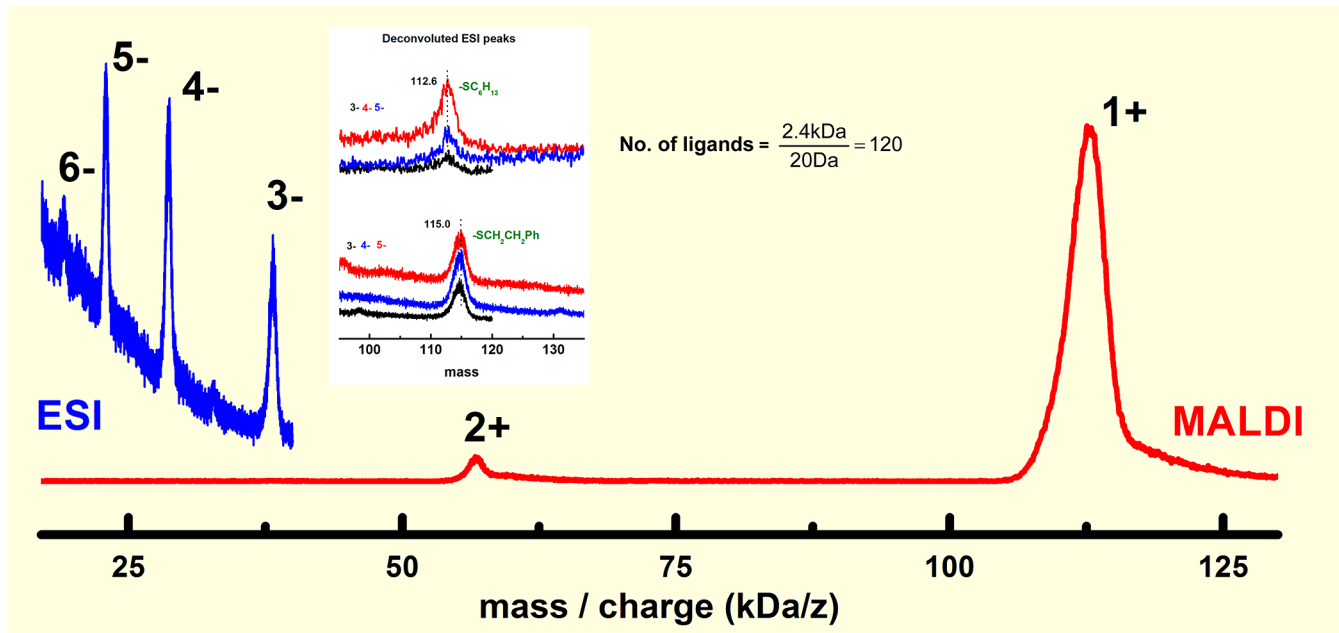


Figure 1. Mass Spectrometry. MALDI (red) and ESI (blue) mass spectra of “115 kDa” nanoparticles yielding a composition of $\text{Au}_{\sim 500 \pm 10}(\text{SCH}_2\text{CH}_2\text{Ph})_{\sim 120 \pm 3}$. MALDI-MS shows 1+ and 2+ ions, while ESI yields 3-, 4-, 5-, and 6- ions. Deconvolution of the six charged ions is consistent with a 115 kDa molecular ion. The inset shows the deconvoluted spectra of $\text{Au}_{\sim 500}$ protected by $-\text{SCH}_2\text{CH}_2\text{Ph}$ and $-\text{SC}_6\text{H}_{13}$ ligands, where the 3-, 4-, and 5- ESI peaks are multiplied by 3, 4, and 5 to yield the 1- molecular ion, at 115 kDa. From the mass difference, the total number of ligands was calculated to be 120.

High resolution mass analysis was performed using ESI-MS. Electrospray ionization of Faradaurate-500 shows multiply charged peaks at 38.23, 28.62, and 22.97 kDa corresponding to the 3-, 4-, and 5- intact ions, respectively. The ESI peaks exhibit broad features as shown in Figure 1. This is due to the presence of several stable species and/or gold thiol combinations. The observed mass peaks suggest the existence of at least 20 intact species in the 115 kDa mass range, and the composition of the Faradaurates was assigned to be $\text{Au}_{\sim 500}(\text{SCH}_2\text{CH}_2\text{Ph})_{\sim 120}$. The composition was confirmed by the mass difference found when preparing the nanoparticles using another ligand (HSC₆H₁₃). In this case, ESI-MS of nanoparticles with two ligands of varying mass yields the number of ligand molecules. On the basis of the number of ligand molecules, the total number of metal atoms could be calculated. All of the above evidence supports a composition of $\text{Au}_{\sim 500}(\text{SR})_{\sim 120}$. The width of the peak was analyzed to get an estimate of the number of species present, yielding a composition of $\text{Au}_{\sim 500 \pm 10}(\text{SCH}_2\text{CH}_2\text{Ph})_{\sim 120 \pm 3}$, as discussed further below.

High Energy X-ray Scattering and PDF Analysis. High energy X-ray total scattering measurements include both Bragg and diffuse contributions to the scattering intensity. Fourier transformation of the background corrected data to real space yields the PDF.^{25,26} The atomic PDF provides a histogram of all the atom–atom distances in a material. The PDF method has significant advantages over other local structural probes, such as X-ray absorption spectroscopy (XAS):²⁷ there is negligible radiation damage of the sample as the monochromatic high-energy X-rays (>60 keV) are weakly absorbed; data is obtained at longer length scales (>10 Å) compared to X-ray absorption spectroscopy (XAS), yielding insights into size, shape, and atomic arrangement; the interatomic distances measured are absolute and can be compared with the PDFs calculated for structural models.

Figure 2 shows the atomic PDF patterns of the Faradaurate-500 compound. To evaluate the structure, we compared the experimental data with PDF of icosahedral, decahedral, and fcc shapes. The Au_{309} icosahedron and Au_{389} Marks decahedron were selected as their size is closer to that of the metallic core with a shell of Au adatoms in the form of -SR-Au-SR- units. To represent cubic closed packing, we chose the 100 nm Au nanoparticle purchased from Sigma-Aldrich, which has a bulk-like fcc structure. Comparing the experimental PDF of $\text{Au}_{\sim 500}$ with various models in Figure 2 shows that there is a poor match with Au_{309} icosahedron. Therefore, we conclude that an icosahedral core is unlikely. However, the experimental PDF of $\text{Au}_{\sim 500}$ equally matches both the Au_{389} Marks decahedron (Dh) model and the 100 nm Au NP with a bulk-like fcc structure.

In addition to atomic structure insights via PDF, information about the nanoparticle size can also be obtained by modeling how the intensity of features in the PDF at longer distances attenuate. The longest interatomic distances observed in the PDF, at ~2.4 nm, correspond to the size/diameter of the particles. This is in agreement with the size measurements from HAADF-STEM images shown in Figure 3. The PDFs were dominated by atom–atom correlations associated with Au–Au interactions; Au–S and other correlations involving more weakly scattering carbon and hydrogen atoms did not contribute significantly to the measured PDFs. Features in the PDF of the $\text{Au}_{\sim 500}$ sample extended to 25 Å, while longer range features are observed in 100 nm particles.

Considering the total number of Au atoms and assuming monomeric [-SR-Au-SR-] arrangement for the interface, we propose the Au_{405} and Au_{389} core for the $\text{Au}_{\sim 500}(\text{SR})_{\sim 120}$ particles, which contain the 5-shell structure (4-shells of core and an outermost shell with [-SR-Au-SR-] bonding).

Scanning Transmission Electron Microscopy Analysis.

Direct imaging of the gold nanoparticles of less than 5 nm diameter is challenging due to the electron beam induced

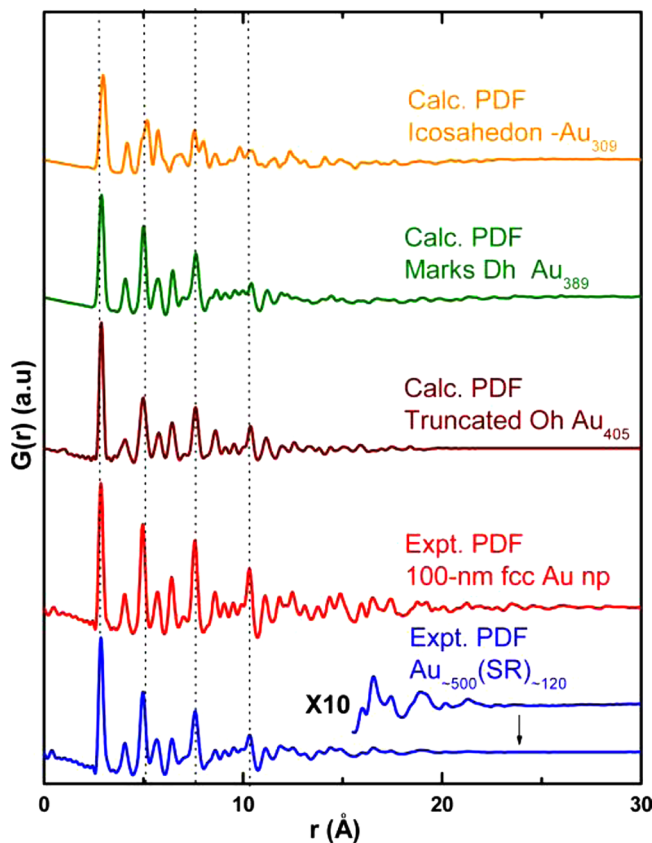


Figure 2. Experimental atomic PDF of $\text{Au}_{\sim 500 \pm 10}(\text{SR})_{120 \pm 3}$ in comparison with calculated PDF patterns of icosahedral Au_{309} , Marks Dh Au_{389} , Truncated Oh Au_{405} and 100 nm fcc (bulk like) patterns. PDF patterns of $\text{Au}_{\sim 500}$ show a decent match with Marks Dh and fcc patterns.

instability and dynamic aggregation and sintering.²⁸ This may lead to changes in the atomic structure and can limit the analysis of the degree of size homogeneity, nanoparticle shape, and individual particle size. Here we show low-magnification and high-resolution HAADF-STEM images of the $\text{Au}_{\sim 500}(\text{SR})_{\sim 120}$ particles, to study both the size dispersity and the atomic structure. The low-magnification images in Figure 3a,b present representative ensembles of particles, including regions of self-assembly (see expansion in Figure 3c).

The self-assembled particles demonstrate the size-selected and monodisperse nature of the sample. The other regions show isolated particles that are well separated from each other. Figure 3d–h show the aberration-corrected HAADF-STEM images of the $\text{Au}_{\sim 500}(\text{SR})_{\sim 120}$ nanoparticles. These high-resolution images illustrate the arrays of surface atoms on the particles, in addition to their size and shape. By observing single particles at different orientations one can, in principle, study the surface morphology of the individual $\text{Au}_{\sim 500}(\text{SR})_{\sim 120}$ nanoparticles. This is because the intensity of the HAADF-STEM image is dependent on both atomic number and number of atoms in each atomic column. However, rapid surface atom diffusion or loss, and reconstruction, is often observed under the high dose rate required for high-resolution imaging. The electron beam can also induce a change in particle size and shape.²⁸ Therefore, care was taken to try to minimize dose ($4 \times 10^4 \text{ e}^-/\text{\AA}^2$), and only first-pass images were used in the analysis.

Images in Figure 3d,g,h seem to suggest an fcc shape, while images in Figure 3e,f are ambiguous and may have other shapes. Different particle shapes were observed, due to the random orientation of the $\text{Au}_{\sim 500}(\text{SR})_{\sim 120}$ clusters on the substrate. PDF fitting was performed with Au_{405} truncated octahedral and Au_{389} Marks decahedral model using PDFgui. On the basis of both PDF fits (Figure 4) and HAADF-STEM data, we conclude that Au_{405} truncated octahedra and Au_{389} Marks decahedron models are the most probable structures for the inner core of the $\text{Au}_{\sim 500}$ nanoparticle. A more systematic study

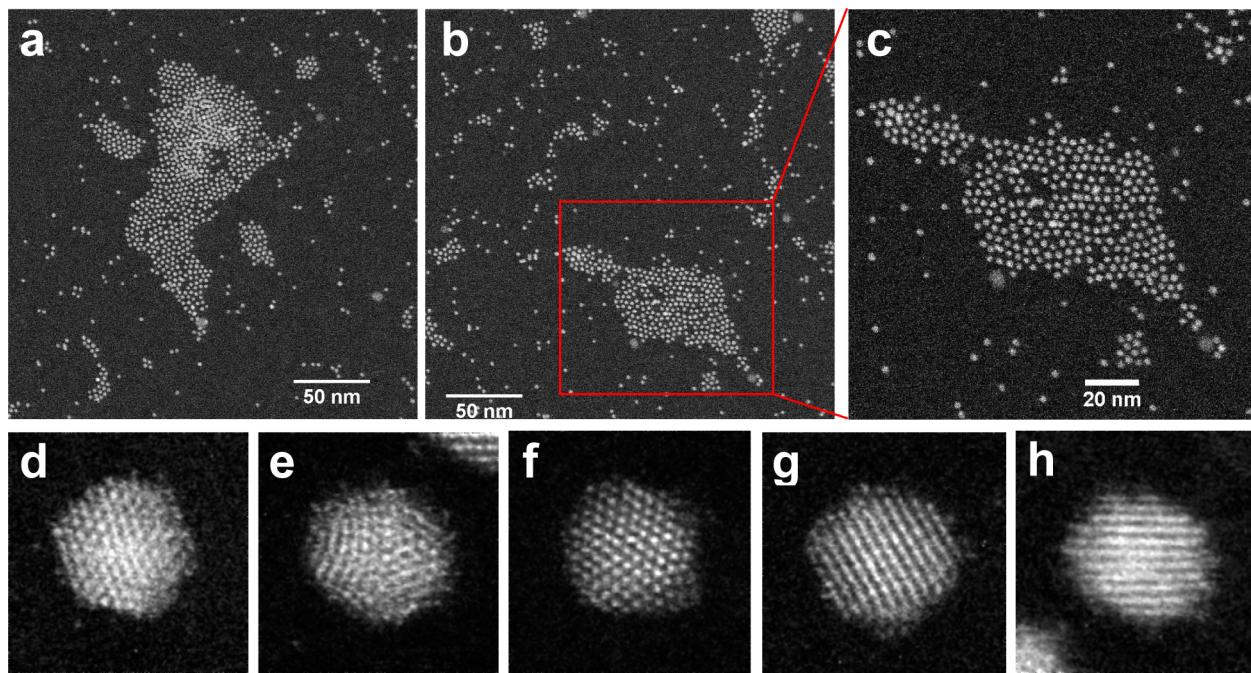


Figure 3. HAADF-STEM images of $\text{Au}_{\sim 500}(\text{SR})_{\sim 120}$. (a–c) Low-magnification images of dispersed $\text{Au}_{\sim 500}$. (d–h) High-resolution images of individual particles, field of view is $5 \text{ nm} \times 5 \text{ nm}$. See related discussion in the text.

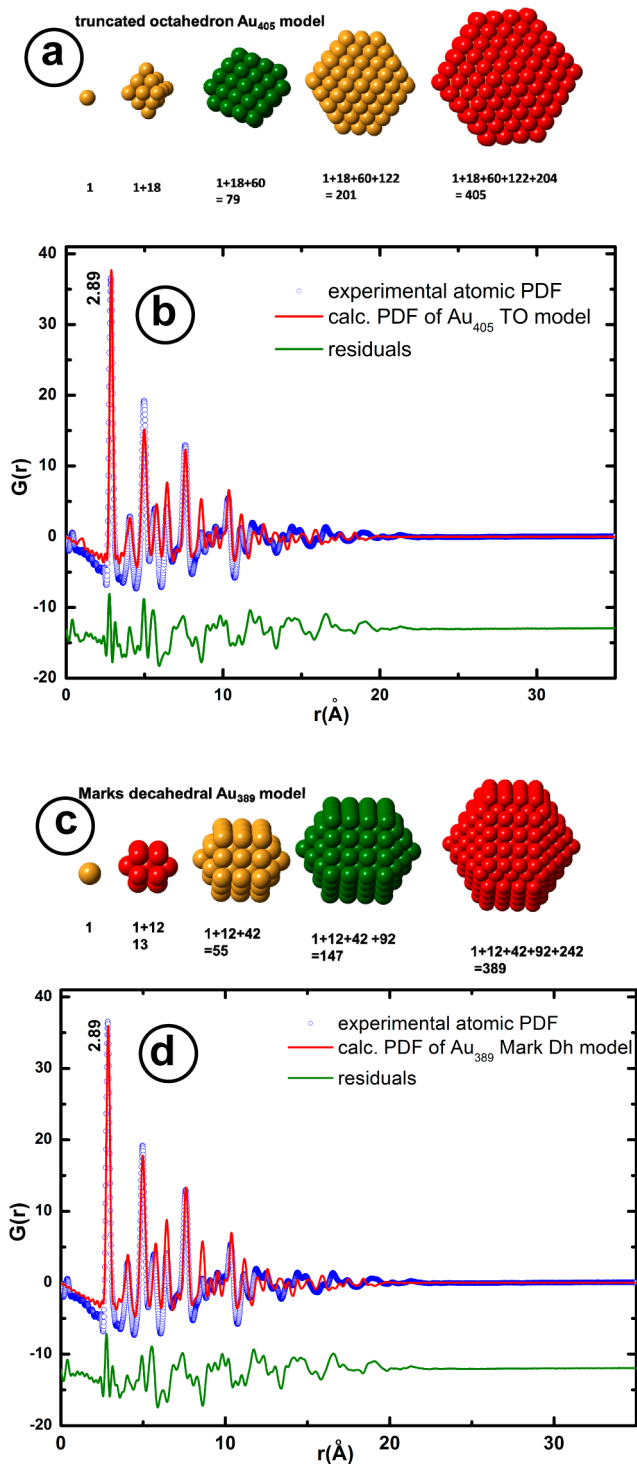


Figure 4. PDF fits. (a) Truncated octahedral Au_{405} model, (b) PDF fitting of Au_{405} TO model with that of the experimental PDF of $\text{Au}_{\sim 500}(\text{SR})_{\sim 120}$ particles ($R_w = 37\%$). (c) Marks decahedral Au_{389} model, (d) PDF fitting of Au_{389} Marks Dh model with that of the experimental PDF of $\text{Au}_{\sim 500}(\text{SR})_{\sim 120}$ particles ($R_w = 23\%$).

with a statistically significant number of atomic resolution HAADF-STEM images will aid in more conclusive atomic structure information.

Small Angle X-ray Scattering (SAXS). Figure 5a shows the SAXS data for $\text{Au}_{\sim 500}$. SAXS provides independent, statistically representative, ensemble measurements of the size and conformation of nanoparticles. The radius of gyration, R_g ,

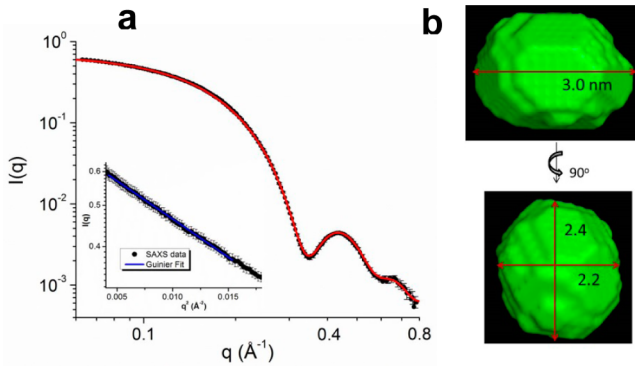


Figure 5. SAXS data, data fits, and the derived SAXS molecular envelope for $\text{Au}_{\sim 500}$ nanoparticles. (a) SAXS data (black solid circle with error bar) were collected up to 0.8\AA^{-1} . The red curve is a representative fit for the molecular envelope calculation. The molecular envelope, also known as a bead model, was calculated using the program DAMMIN, with SAXS data up to 0.6\AA^{-1} . The data points in the red curve beyond 0.6\AA^{-1} were calculated from the resultant molecular envelope, matching well with the experimental data. The inset is the Guinier fit for SAXS data at q close to 0. R_g obtained from the data fit is $1.05 \pm 0.05 \text{ nm}$. (b) The two views of the final SAXS molecular envelope with dimensions. Twenty independent molecular envelope calculations were performed, and the resulting envelopes were further averaged to generate the final, consensus molecular envelope. The error bar of the dimensions is expected as $0.1\text{--}0.2 \text{ nm}$.

of the nanoparticles obtained from the SAXS Guinier fit, i.e., $\ln[I(q)] = \ln[I(q=0)] - R_g^2 q^2 / 3$ at q close to zero, is $1.05 \pm 0.05 \text{ nm}$. The wide range of linear Guinier behavior ($\ln[I(q)]$ vs q^2 , Figure 5a inset) and the scattering oscillation features at a q of $0.3\text{--}0.8 \text{\AA}^{-1}$ strongly suggest that the $\text{Au}_{\sim 500}$ nanoparticles are nearly monodisperse in solution. However, a simple spherical model, including a size distribution, was unable to fit the data. We reconstructed a three-dimensional molecular envelope directly from the SAXS data using an ab initio program DAMMIN,²⁹ and this SAXS envelope adopts an ellipsoid-like shape with dimensions in the range of $2.2\text{--}3.0 \text{ nm}$, displayed in Figure 5b. This SAXS molecular envelope is consistent with the HAADF-STEM images, in terms of shape and size, and interestingly, it also exhibits facet features. It should be pointed out that since the electron density of the SR ligand is much less than that of the Au-cluster core, the SAXS data and the molecular envelope are dominated by the contribution from the $\text{Au}_{\sim 500}$ nanoparticle core.

UV–Visible Spectra. Figure 6 presents the UV–visible–NIR absorption spectra of the $\text{Au}_{\sim 500}(\text{SR})_{\sim 120}$ in comparison with other reported nanomolecules with 38– and 144– atoms, as well as the plasmonic 76 kDa species. The bottom spectrum shows the molecule-like transition of $\text{Au}_{38}(\text{SR})_{24}$ nanomolecules. The optical spectrum of $\text{Au}_{144}(\text{SR})_{60}$ shows the discrete electronic states of the nanoparticles, but due to the overlap of various electronic transitions, it appears featureless. However, recent studies show that the origin of localized surface plasmon resonance of the $\text{Au}_{144}(\text{SR})_{60}$ is confined to the metallic core.^{30,31} The $\text{Au}_{329}(\text{SR})_{84}$ nanomolecules support a distinct surface plasmon resonance (SPR) peak at $\sim 490 \text{ nm}$. This is due to the collective oscillation of the conduction electrons. $\text{Au}_{\sim 500}(\text{SR})_{\sim 120}$ also shows the surface plasmon resonance at $\sim 498 \text{ nm}$. However, this peak is not prominent compared to the 76.3 kDa nanoparticles. This is due to the

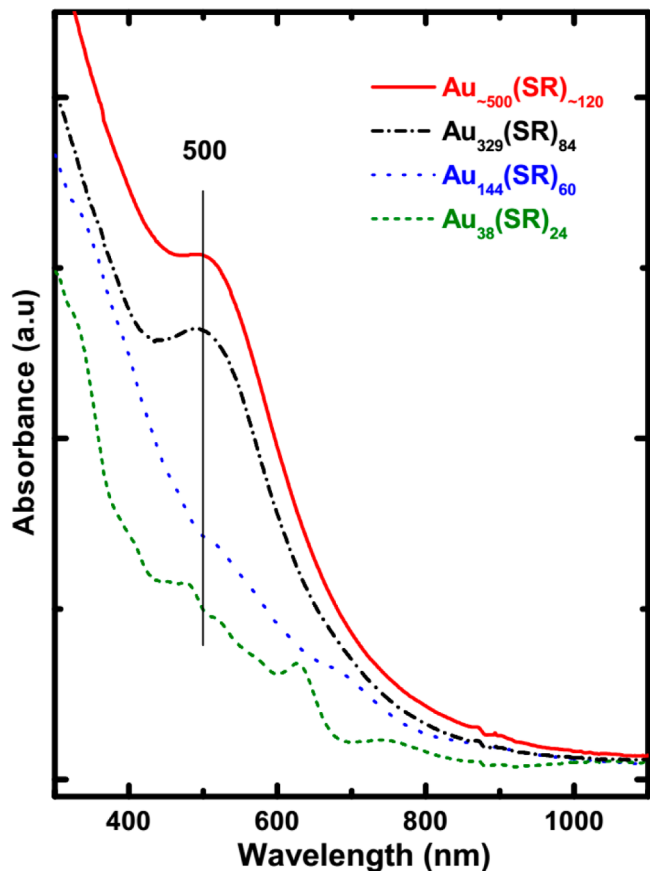


Figure 6. UV-visible-NIR spectroscopy of $\text{Au}_{\sim 500}(\text{SR})_{\sim 120}$ (red) showing the surface plasmon resonance peak at $\sim 498 \text{ nm}$ compared to the 76.3 kDa, $\text{Au}_{329}(\text{SR})_{84}$ (black dash dotted). $\text{Au}_{144}(\text{SR})_{60}$ (blue dotted) shows no surface plasmon resonance, and $\text{Au}_{38}(\text{SR})_{24}$ (green dashed) shows molecule-like transitions.

presence of several overlapping stable species, which show SPR in the 480–510 nm range.

Size Polydispersity. Finally, we analyze the width of the mass spectra to determine the size dispersity. For this purpose, we intentionally mixed the 76.3 kDa species²⁴ with that of the title $\text{Au}_{\sim 500}$ nanoparticle. We have recently shown that the 76.3 kDa species has one fixed composition, with a $\text{Au}_{329}(\text{SR})_{84}$ formula, with no variation in the number of Au atoms and ligands.³²

Comparing the mass spectra of a mixture of $\text{Au}_{329}(\text{SR})_{84}$ and $\text{Au}_{\sim 500}$ species in Figure 7a shows that there is a large difference in the peak width and full width at half-maximum (fwhm). Figure 7b shows the expanded version of the 5– of the $\text{Au}_{\sim 500}$ and the 3– of the $\text{Au}_{329}(\text{SR})_{84}$. The width of the 5– of the $\text{Au}_{\sim 500}$ peak at the baseline is approximately 800 m/z. Deconvolution of this peak to the molecular 1– ion leads to a width of 4000 Da. In the extreme case, where the entire 4000 Da difference is due to Au atoms, a variation of 20 Au atoms would be observed. If the entire mass is due to ligands, then it would lead to a variation of 29 ligands. Nevertheless, a more accurate prediction is to calculate the percent variation of Au atoms ($20/500 = 4\%$) and apply it to ligands. This would lead to a reasonable variation of ($120 \times 0.04 = 5$) five ligands. Also, note that the expanded 5– peaks show ~ 30 partially resolved individual peaks within the envelope. We therefore conclude that the composition of the title compound to be

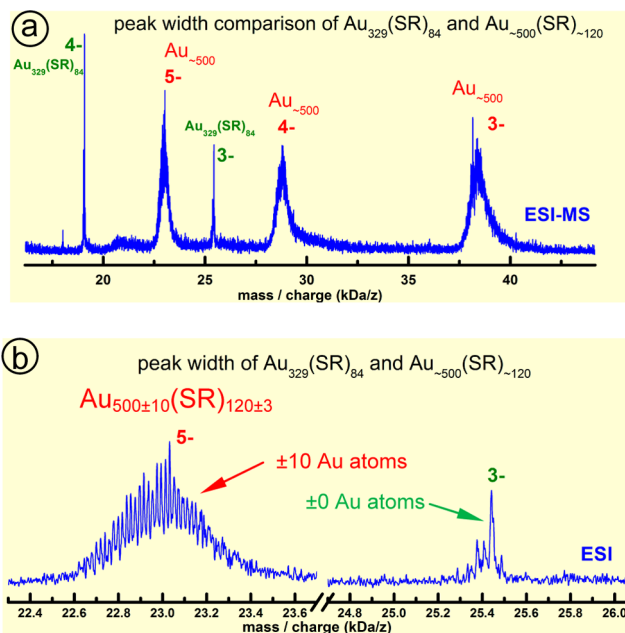


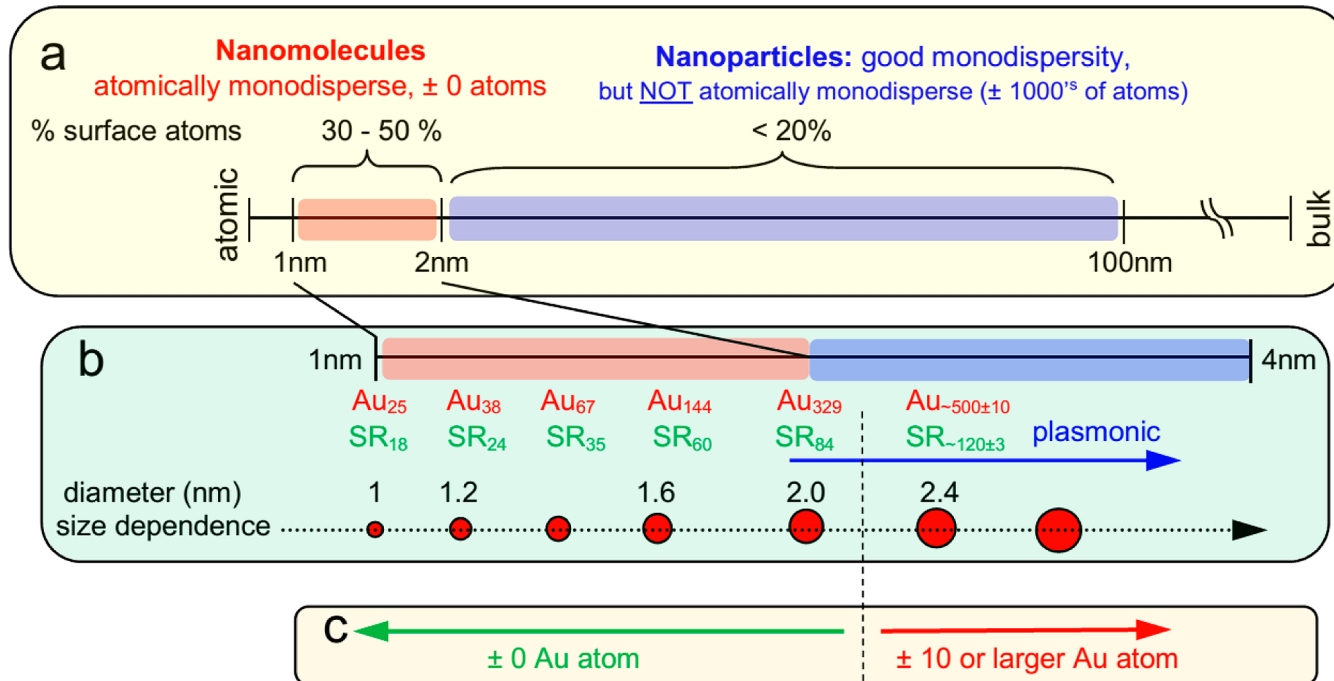
Figure 7. (a) ESI-MS of $\text{Au}_{329}(\text{SR})_{84}$ and $\text{Au}_{\sim 500}$ nanoparticles that were intentionally mixed to study the peak width and size dispersity. Note the sharp peaks for $\text{Au}_{329}(\text{SR})_{84}$ when compared with the $\text{Au}_{\sim 500}$ peaks. (b) Expansion of the 5– peak of $\text{Au}_{\sim 500}$ and the 3– peak of the $\text{Au}_{329}(\text{SR})_{84}$. The fwhm of the 3– peak of $\text{Au}_{329}(\text{SR})_{84}$ is 23 m/z suggesting that it is a fixed composition, with ± 0 atom variation (see ref 32). The $\text{Au}_{\sim 500}$ nanoparticle is broad (fwhm of 800 m/z) and shows overlap of several peaks, suggesting a size dispersity of approximately 20 Au atoms.

$\text{Au}_{\sim 500 \pm 10}(\text{SR})_{\sim 120 \pm 3}$ with over 30 individual $\text{Au}_m(\text{SR})_n$ species present.

Transition from Fixed-Composition to Polydisperse Nature.

Nanomolecules protected by aliphatic thiol or phenylethanethiol include $\text{Au}_{25}(\text{SR})_{18}$, $\text{Au}_{38}(\text{SR})_{24}$, $\text{Au}_{67}(\text{SR})_{35}$, $\text{Au}_{130}(\text{SR})_{50}$, $\text{Au}_{144}(\text{SR})_{60}$, and $\text{Au}_{329}(\text{SR})_{84}$. These have a molecular definition with ± 0 Au atom or ligand variation. The only ultrasmall, <2 nm-sized phenylethanethiol-protected nanoparticle that does not have a molecular definition is the $\text{Au}_{103-105}(\text{SR})_{45-46}$ species.³³ However, this species, upon thermochemical treatment at 80 °C, is unstable, resulting in a core size conversion that produces a new core size, $\text{Au}_{40}(\text{SR})_{24}$.³⁴ Nanomolecules that are stable under 80 °C thermochemical excess thiol treatment include the 25–, 38–, 130–, 144–, and 329– atom species. The Faradaurate-500 species is also highly stable because its synthesis involves a 80 °C thermochemical treatment for 4–7 days. However, the highly stable Faradaurate-500 does not contain a single species with a fixed composition. It contains at least 30 different nanoparticle compositions. Significant efforts were made to acquire the ESI-MS data under “soft” conditions to minimize fragmentation. Several control experiments of known nanomolecules performed under similar conditions were free to fragmentation. On the basis of the above results in Figure 7, we conclude that an *important transition from a fixed composition to a polydisperse composition occurs within the 329– and 500– atom range*. See Scheme 1. In the nanoparticle regime below <500 atoms, there are well studied molecular particles like $\text{Au}_{25}(\text{SR})_{18}$, $\text{Au}_{38}(\text{SR})_{24}$, $\text{Au}_{144}(\text{SR})_{60}$, and $\text{Au}_{329}(\text{SR})_{84}$.

Exemplary Stability. Note that these sizes are extremely stable in air, and under thermochemical treatment at 80 °C in

Scheme 1^a

^a(a) The 1–100 nm regime with nanomolecules in the 1–2 nm region, and nanoparticles in the 2–100 nm regime (where very good monodispersity has been achieved, but the size distribution is still ± 1000 's of atoms or a few nanometers). (b) Thiolated gold nanomolecules, such as Au_{25} , Au_{38} , Au_{67} , Au_{144} , and Au_{329} with a precise number of metal atoms and organic ligands and $\text{Au}_{\sim 500 \pm 10}(\text{SR})_{\sim 120 \pm 3}$. (c) The dashed line, between 329– and 500– atom sizes, indicating the transition between the fixed composition containing nanomolecules region, with ± 0 Au atom variation versus polydisperse $\text{Au}_{\sim 500 \pm 10}(\text{SR})_{\sim 120 \pm 3}$ particles, with a ± 10 Au atom variation.

Table 1. Properties of $\text{Au}_{\sim 500}(\text{SR})_{\sim 120}$ as Determined from the Comprehensive Suite of Analytical Tools

composition ^a	SAXS diameter (nm)	TEM diameter (nm)	atomic structure ^b	$\text{Abs}_{\text{max}}^{\text{(nm)}} (\text{M}^{-1} \text{cm}^{-1})$
$\text{Au}_{\sim 500}(\text{SR})_{\sim 120}$	2.6 ± 0.4	2.4 ± 0.1	~ 2.5 dia. (nm) cubic close packed, truncated octahedral/marks decahedron	$498, 1.42 \times 10^6$

^aFrom mass spectrometry. ^bAtomic pair distribution function analysis.

excess thiol. Nevertheless, the $\text{Au}_{\sim 500}$ nanoparticle, which underwent 80 °C thermochemical treatment for several days, still remains polydisperse with a composition of $\text{Au}_{\sim 500 \pm 10}(\text{SR})_{\sim 120 \pm 3}$. The superatom model³⁵ relies on electronic stability due to closed electronic shells. Based on the fact that there is not a fixed composition in the title compound, it can therefore be concluded that $\text{Au}_{\sim 500}$ is not stabilized due to electronic considerations. This would suggest that geometric stability³⁶ plays a more significant role in the stability of Faradaurate-500. $\text{Au}_{25}(\text{SR})_{18}^-$ and $\text{Au}_{102}(\text{SPh-COOH})_{44}$ are stabilized by two factors: (a) electronic factors exhibiting 8 and 58 electron shell closings, respectively; (b) geometric factors exhibiting a 13– atom icosahedral core and a 49– atom Marks decahedral core, respectively. Note that $\text{Au}_{144}(\text{SR})_{60}$ and $\text{Au}_{329}(\text{SR})_{84}$ has 84 and 245 electrons, respectively. So none of the species in the Faradaurate series, namely, 144–, 329–, and ~ 500 – atom species, exhibit electronic shell closings. This suggests that as the nanoparticle size increases, the geometry plays a larger role in the nanoparticle stability. However, as the size increases, there are apparently various possible combinations that would lead to a stable nanoparticle (Table 1).

CONCLUSIONS

In summary, we have determined the composition of the plasmonic Faradaurate at 115 kDa as $\text{Au}_{\sim 500}(\text{SR})_{\sim 120}$. HAADF-STEM imaging shows that the particles are monodisperse and the diameter is 2.4 ± 0.1 nm. SAXS results support the monodispersity and the particle diameter was determined to be 2.6 nm, in agreement with the STEM analysis. High-energy X-ray PDF analysis suggests that the atomic structure of Faradaurate-500 is consistent with both an fcc or a Marks decahedral atomic arrangement. Finally, plasmonic peaks for these particles appear at 498 nm. The extinction coefficient was determined to be $1.42 \times 10^6 \text{ M}^{-1} \text{ cm}^{-1}$, which is supported by ~ 380 free electrons. These plasmonic nanoparticles can be used in plasmonic applications such as optical sensors, drug delivery, and cancer cell detection and also in catalytic applications.

AUTHOR INFORMATION

Corresponding Author

amal@olemiss.edu

Notes

The authors declare no competing financial interest.

ACKNOWLEDGMENTS

A.D. and C.K. were funded through NSF-CHE-1255519. Work performed at Argonne and use of the Advanced Photon Source, an Office of Science User Facility operated for the U.S. Department of Energy (DOE) Office of Science by Argonne National Laboratory, was supported by the U.S. DOE under Contract No. DE-AC02-06CH11357. Electron microscopy was supported through a user project at ORNL's Center for Nanophase Materials Sciences (CNMS), which is sponsored by the Scientific User Facilities Division, Office of Basic Energy Sciences, U.S. Department of Energy. We thank Riccardo Ferrando for assistance with theoretical models and Miguel Yacaman, Robert Whetten, and Daniel Bahenas for preliminary STEM results. We thank Pavol Juhas for help with python script used in calculating atomic PDF.

REFERENCES

- (1) Rycenga, M.; Cobley, C. M.; Zeng, J.; Li, W.; Moran, C. H.; Zhang, Q.; Qin, D.; Xia, Y. *Chem. Rev.* **2011**, *111*, 3669–3712.
- (2) Rand, B. P.; Peumans, P.; Forrest, S. R. *J. Appl. Phys.* **2004**, *96*, 7519–7526.
- (3) Khoo, S. Y.; Yang, H.; He, Z.; Miao, J.; Leong, K. C.; Li, C. M.; Yang Tan, T. T. *J. Mater. Chem. C* **2013**, *1*, 5402–5409.
- (4) Pudasaini, P. R.; Ayon, A. A. *Phys. Status Solidi A* **2012**, *209*, 1475–1480.
- (5) Dingwen, Z.; Milton, W.; Alexandre, G. B.; Jie, S.; Xiaodong, L.; Sumei, H. *J. Phys. D: Appl. Phys.* **2013**, *46*, 024005.
- (6) Khlebtsov, N. G.; Dykman, L. A. *J. Quant. Spectrosc. Radiat. Transfer* **2010**, *111*, 1–35.
- (7) Luo, Y. *Mater. Lett.* **2007**, *61*, 1039–1041.
- (8) Palui, G.; Ray, S.; Banerjee, A. *J. Mater. Chem.* **2009**, *19*, 3457–3468.
- (9) Chen, Y.; Gu, X.; Nie, C.-G.; Jiang, Z.-Y.; Xie, Z.-X.; Lin, C.-J. *Chem. Commun.* **2005**, 4181–4183.
- (10) Brust, M.; Walker, M.; Bethell, D.; Schiffrin, D. J.; Whyman, R. J. *Chem. Soc., Chem. Commun.* **1994**, 801–802.
- (11) Schaaff, T. G.; Whetten, R. L. *J. Phys. Chem. B* **1999**, *103*, 9394–9396.
- (12) Whetten, R. L.; Khouri, J. T.; Alvarez, M. M.; Murthy, S.; Vezmar, I.; Wang, Z. L.; Stephens, P. W.; Cleveland, C. L.; Luedtke, W. D.; Landman, U. *Adv. Mater.* **1996**, *8*, 428–433.
- (13) Dass, A.; Stevenson, A.; Dubay, G. R.; Tracy, J. B.; Murray, R. W. *J. Am. Chem. Soc.* **2008**, *130*, 5940–5946.
- (14) Negishi, Y.; Sakamoto, C.; Ohyama, T.; Tsukuda, T. *J. Phys. Chem. Lett.* **2012**, *3*, 1624–1628.
- (15) Chaki, N. K.; Negishi, Y.; Tsunoyama, H.; Shichibu, Y.; Tsukuda, T. *J. Am. Chem. Soc.* **2008**, *130*, 8608–8610.
- (16) Nimmala, P. R.; Yoon, B.; Whetten, R. L.; Landman, U.; Dass, A. *J. Phys. Chem. A* **2013**, *117*, 504–517.
- (17) Harkness, K. M.; Tang, Y.; Dass, A.; Pan, J.; Kothalawala, N.; Reddy, V. J.; Cliffel, D. E.; Demeler, B.; Stellacci, F.; Bakr, O. M.; McLean, J. A. *Nanoscale* **2012**, *4*, 4269–4274.
- (18) Kumara, C.; Dass, A. *Nanoscale* **2012**, *4*, 4084–4086.
- (19) Kumara, C.; Dass, A. *Nanoscale* **2011**, *3*, 3064–3067.
- (20) Jadzinsky, P. D.; Calero, G.; Ackerson, C. J.; Bushnell, D. A.; Kornberg, R. D. *Science* **2007**, *318*, 430–433.
- (21) Qian, H.; Eckenhoff, W. T.; Zhu, Y.; Pintauer, T.; Jin, R. *J. Am. Chem. Soc.* **2010**, *132*, 8280–8281.
- (22) Heaven, M. W.; Dass, A.; White, P. S.; Holt, K. M.; Murray, R. W. *J. Am. Chem. Soc.* **2008**, *130*, 3754–3755.
- (23) Kumara, C.; Aikens, C. M.; Dass, A. *J. Phys. Chem. Lett.* **2014**, *5*, 461–466.
- (24) Dass, A. *J. Am. Chem. Soc.* **2011**, *133*, 19259–19261.
- (25) Egami, T.; Billinge, S. J. L. *Underneath the Bragg Peaks: Structural Analysis of Complex Materials*; Elsevier: Oxford, U.K., 2003.
- (26) Billinge, S. J. L.; Levin, I. *Science* **2007**, *316*, 561–565.
- (27) Chupas, P. J.; Chapman, K. W.; Jennings, G.; Lee, P. L.; Grey, C. P. *J. Am. Chem. Soc.* **2007**, *129*, 3822–13824.
- (28) Chen, Y.; Palmer, R. E.; Wilcoxon, J. P. *Langmuir* **2006**, *22*, 2851–2855.
- (29) Svergun, D. I. *Biophys. J.* **1999**, *76*, 2879–2886.
- (30) Malola, S.; Lehtovaara, L.; Enkovaara, J.; Häkkinen, H. *ACS Nano* **2013**, *7*, 10263–10270.
- (31) Yi, C.; Tofanelli, M. A.; Ackerson, C. J.; Knappenberger, K. L. *J. Am. Chem. Soc.* **2013**, *135*, 18222–18228.
- (32) Kumara, C.; Dass, A. *Anal. Chem.* **2014**, DOI: 10.1021/ac403851s.
- (33) Dass, A.; Nimmala, P. R.; Jupally, V. R.; Kothalawala, N. *Nanoscale* **2013**, *5*, 12082–12085.
- (34) Nimmala, P. R.; Jupally, V. R.; Dass, A. *Langmuir* **2014**, *30*, 2490–2497.
- (35) Walter, M.; Akola, J.; Lopez-Acevedo, O.; Jadzinsky, P. D.; Calero, G.; Ackerson, C. J.; Whetten, R. L.; Grönbeck, H.; Häkkinen, H. *Proc. Natl. Acad. Sci. U. S. A.* **2008**, *105*, 9157–9162.
- (36) Dass, A. *Nanoscale* **2012**, *4*, 2260–2263.
- (37) Qiu, X.; Bozin, E. S.; Juhas, P.; Proffen, T.; Billinge, S. J. L. *J. Appl. Crystallogr.* **2004**, *37*, 110–116.
- (38) Chupas, P. J.; Qiu, X.; Hanson, J. C.; Lee, P. L.; Grey, C. P.; Billinge, S. J. L. *J. Appl. Crystallogr.* **2003**, *36*, 1342–1347.
- (39) Ilavsky, J.; Jemian, P. R. *J. Appl. Crystallogr.* **2009**, *42*, 347–353.